Supporting Information for

Highly Branched Ultrathin Pt-Ru Nanodendrites

Ke Guo, Ying Liu, Min Han, Dongdong Xu*, and Jianchun Bao*

Jiangsu Key Laboratory of New Power Batteries, Jiangsu Collaborative Innovation Center of Biomedical Functional Materials, School of Chemistry and Materials Science, Nanjing Normal University, Nanjing, 210023, P. R. China.

*E-mail: ddxu@njnu.edu.cn; baojianchun@njnu.edu.cn

Experimental Sections

Chemicals

Chloroplatinic acid hexahydrate ($H_2PtCl_6·6H_2O$, 99.9 wt%), iron (III) nitrate nonahydrate ($Fe(NO_3)_3·9H_2O$, 99.9 wt%), silver nitrate ($AgNO_3$, 99.9 wt%), L-ascorbic acid (AA) (99%), and commercial platinum (20 wt% on carbon black) were purchased from Alfa Aesar. Ammonium hexachlororuthenate (IV) ($(NH_4)_2RuCl_6$, 99.9 wt%), ammonium hexachlororhodate (III) ($(NH_4)_3RhCl_6$, 99.9 wt%), and dioctadecyldimethylammonium chloride (DODAC) were purchased from Aladdin Corporation. Cobalt (II) nitrate hexahydrate ($Co(NO_3)_2·6H_2O$, 99.9 wt%), ethanol, acetonitrile, and diethyl ether were obtained from Sinopharm Chemical Reagent Co. Ltd. N,N-dimethyldocosylamine and bromoacetic acid (99%) were purchased from TCI Corporation. All the reagents were of analytical reagent grade and used without further purification.

Synthesis of organic surfactants

The surfactants used in this work were synthesized by the procedures as presented in our previous report.[1] Taking the synthesis of C_{22}N-COOH (Br^-) for an example, 7.6 g of N,N-dimethyldocosylamine (20 mmol), 2.6 g of bromoacetic acid (22 mmol) and acetonitrile (150 ml) were refluxed under 95 ^oC for 20 h. After the removal of solvent, the crude product was washed with diethyl ether several times to remove the unreacted reactants and dried in a Freeze dryer.

Synthesis of ultrathin Pt-Ru nanodendrites

The Pt-Ru NDs were synthesized by the reported procedures.[2] Take the synthesis of $Pt_{90}Ru_{10}$ NDs as an example, 1 mL of H_2PtCl_6 aqueous solution (10 mM) and 0.2 mL of $(NH_4)_2RuCl_6$ (10 mM) was mixed into a vial (20 mL) containing 5 mL of C_{22}N-COOH (Br^-) aqueous solution (10 mM) with the pH value of 12. Then, 1 mL of fresh AA aqueous solution (1.2 M) was rapidly injected into the above mixture under gentle shaking. The reaction solution was kept in an oven at 50 ^oC for 12 h. Finally, the Pt-Ru products were collected by centrifugation and washed several times with ethanol. The synthesis of $Pt_{95}Ru_5$, $Pt_{80}Ru_{20}$, and $Pt_{75}Ru_{25}$ NDs was similar to that of $Pt_{90}Ru_{10}$ NDs except the concentration of precursors.

Synthesis of $Pt_{91}Fe_9$, $Pt_{93}Co_7$, $Pt_{90}Rh_{10}$, $Pt_{90}Ag_{10}$ NDs

The synthesis procedures of $Pt_{91}Fe_9$, $Pt_{93}Co_7$, $Pt_{90}Rh_{10}$, $Pt_{90}Ag_{10}$ NDs were similar to that of $Pt_{90}Ru_{10}$ NDs except the different precursors of $Fe(NO_3)_3·9H_2O$, $Co(NO_3)_2·6H_2O$,$(NH_4)_3RhCl_6$, and $AgNO_3$, respectively.

Synthesis of $Pt_{90}Ru_{10}$ nanowires (NWs) and nanorings (NRs)

$Pt_{90}Ru_{10}$ NWs were synthesized through surfactant dioctadecyldimethylammonium chloride (DODAC) under the reduction by $NaBH_4$. The synthesis solution of $Pt_{90}Ru_{10}$ MSs was similar to $Pt_{90}Ru_{10}$ NDs and the subsequent crystalline growth happened under 80°C.

Electrochemical MOR measurements

Electrocatalytic methanol oxidation reaction tests were performed on the CHI 660E electrochemical analyzer at 25 °C. A three-electrodes system was used for all electrochemical tests, in which glassy carbon electrode (GCE, 0.07065 cm^2) was used as the working electrode, a carbon rod as the counter electrode, and a saturated calomel electrode as the reference electrode. An ink of the catalysts was prepared by mixing 1 mg of nanocatalysts, 4 mg of Valcan XC-72 carbon, 1.5 mL of ethanol and 0.5 mL of H_2O, 50 µL of Nafion solution (5 wt% in alcohol and H_2O) was added and sonicated for 0.5 h. Then, 6 µL of above-prepared ink solution (3 µg of the catalyst) was dropped on the GCE electrode and dried at room temperature before test. Cyclic voltammograms (CVs) were then scanned until the stabilized curves were obtained for further removal of the surfactant in 1.0 M KOH.[3] CVs were used to evaluate the electrochemical surface areas (1.0 M KOH) and activities (1.0 M KOH and 1.0 M methanol) of as-synthesized nanocatalysts. The electrolyte solution was initially purged with N_2 for 30 min to remove O_2 and other gas before test. The electrocatalytic performance was also checked in acidic solution following the similar procedure except for the solution (0.5 M H_2SO_4). Electrochemical active surface areas (ECSAs) of the Pt-based catalysts were calculated by integrating the hydrogen adsorption charge on the cyclic voltammetry (CV) at a scan rate of 50 mV/s. The ECSAs of different catalysts was estimated by measuring the charge associated with H_{upd} adsorption (Q_H) between -0.9 and -0.6 V, and assuming 210 µC cm^{-2} for the adsorbed monolayer of hydrogen on Pt surface (q_H) with the equation of $ECSA = Q_H/(q_H\ m)$ where m is the Pt loading amount on the electrode. The H_{upd} adsorption charge (Q_H) could be determined by $Q_H = 0.5Q$, where Q was the charge in the H_{upd} adsorption/desorption area obtained after double-layer correction.

For CO-stripping tests, the work electrode containing 6 µg of the catalyst was immersed in 1 M KOH solution. Then, CO was purged in the solution for 30 min to achieve the maximum coverage of CO at a fixed potential of 0.15 V (SCE). After that, the electrode was moved into fresh N_2-purged 1.0

M KOH solution for CO-stripping measurements. CO-stripping voltammetry was recorded in the potential range between -0.9 and 0.2 V at a scan rate of 50 mV s^{-1}. CO active areas were obtained from the area of the oxidation peaks of CO_{ads}.

Characterizations

The nanostructures and crystalline features of Pt-Ru nanostructures were studied on a JEOL 2100 and probe aberration-corrected JEM ARM 200F apparatuses at the accelerating voltage of 200 kV with the accelerating voltage of 200 kV (TEM, HRTEM, HAADF-STEM, and elemental mappings). XRD patterns were recorded on the powder samples using a D/max 2500 VL/PC diffractometer (Japan) equipped with graphite-monochromatized Cu Kα radiation. XPS spectrum was performed on a scanning X-ray microprobe (Thermo ESCALAB 250Xi) under Al Kα radiation using C 1s peak (284.8 eV) as a standard. Inductively coupled plasma atomic emission spectroscopy (ICP-AES) was recorded on a NexION 350D.

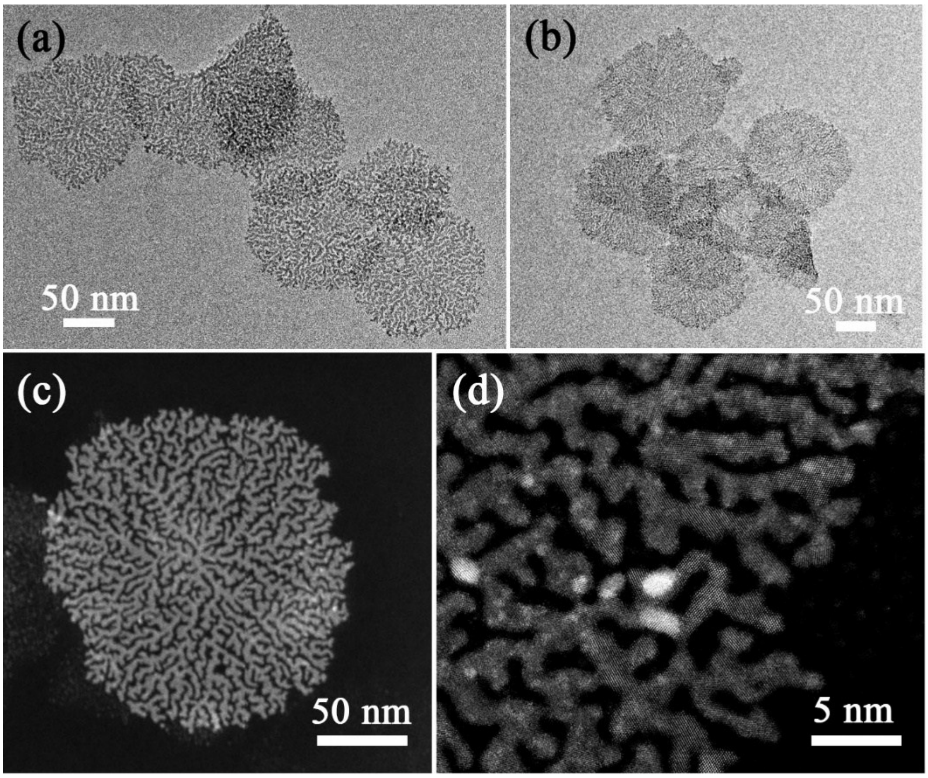

Fig. S1 Additional TEM images (a-b) and HAADF-STEM images (c-d) of highly branched ultrathin Pt-Ru NDs.

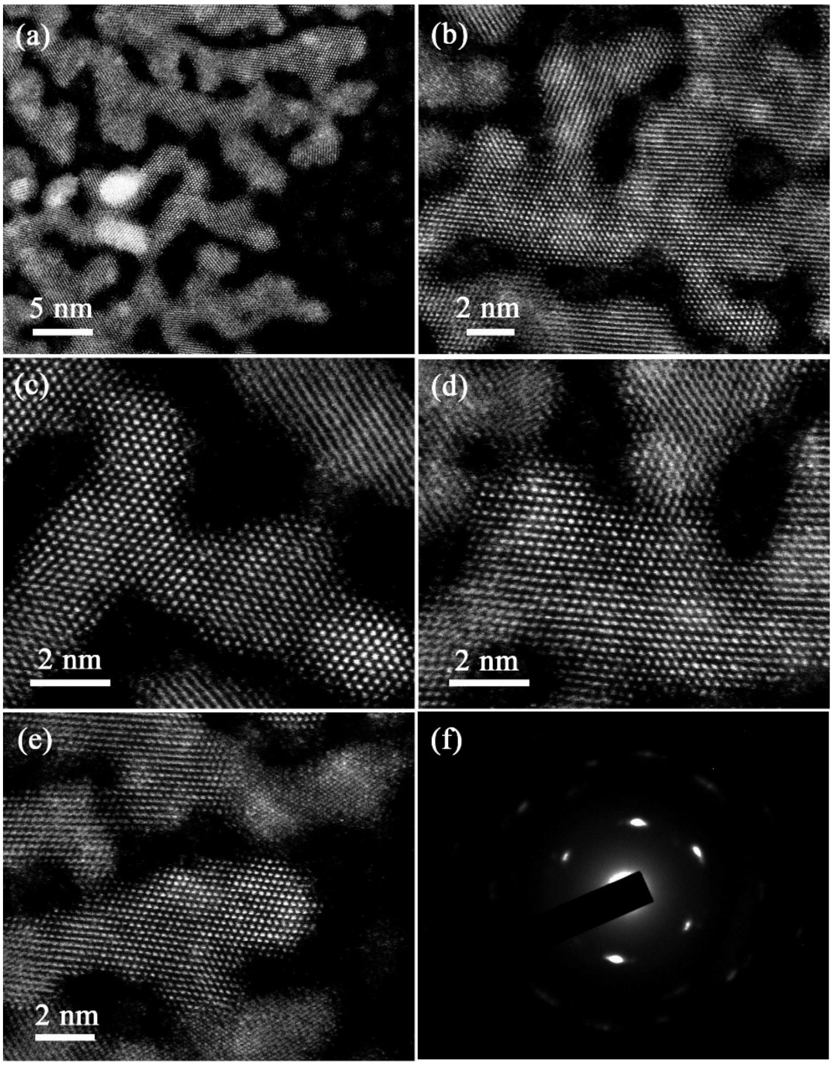

Fig. S2 High-resolution HAADF-STEM images of Pt-Ru NDs (a-e) and SAED pattern (f) taken from an individual Pt-Ru ND indicated the [110] observation direction and the exposed (110) facets. Only one set of diffraction spots declared the single-crystalline feature of Pt-Ru NDs.

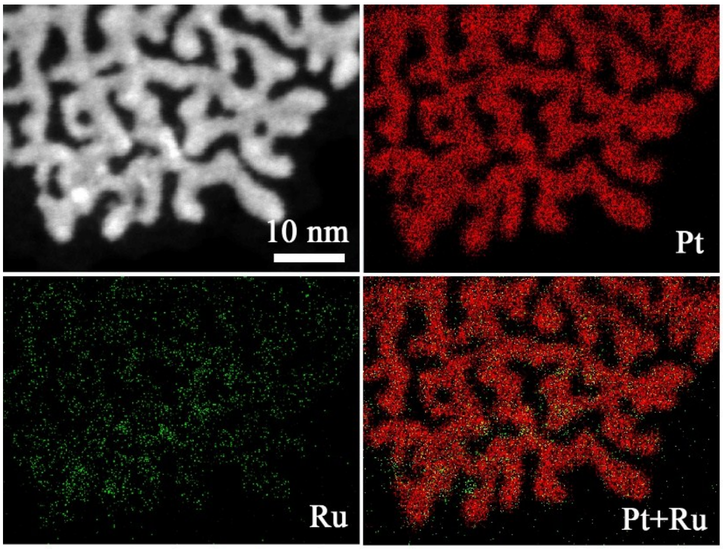

Fig. S3 Additional HAADF-STEM image and corresponding elemental mapping of Pt-Ru NDs.

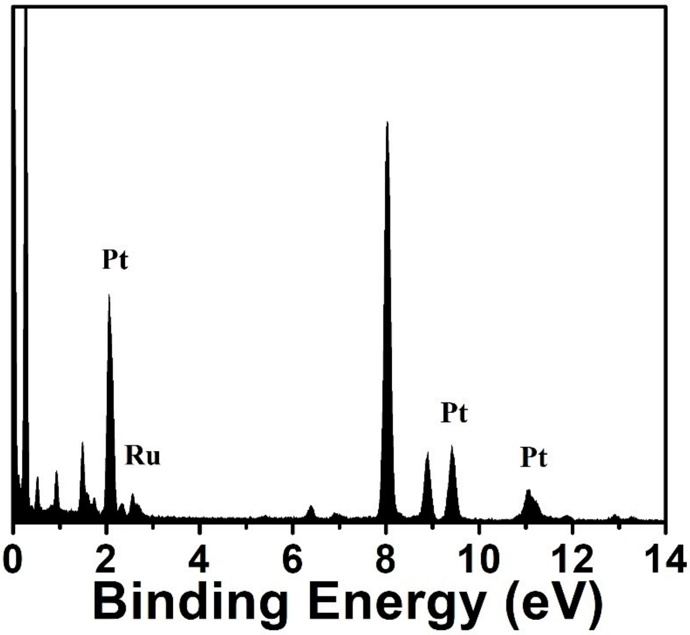

Fig. S4 STEM EDS of ultrathin Pt-Ru NDs presented in Figure 2.

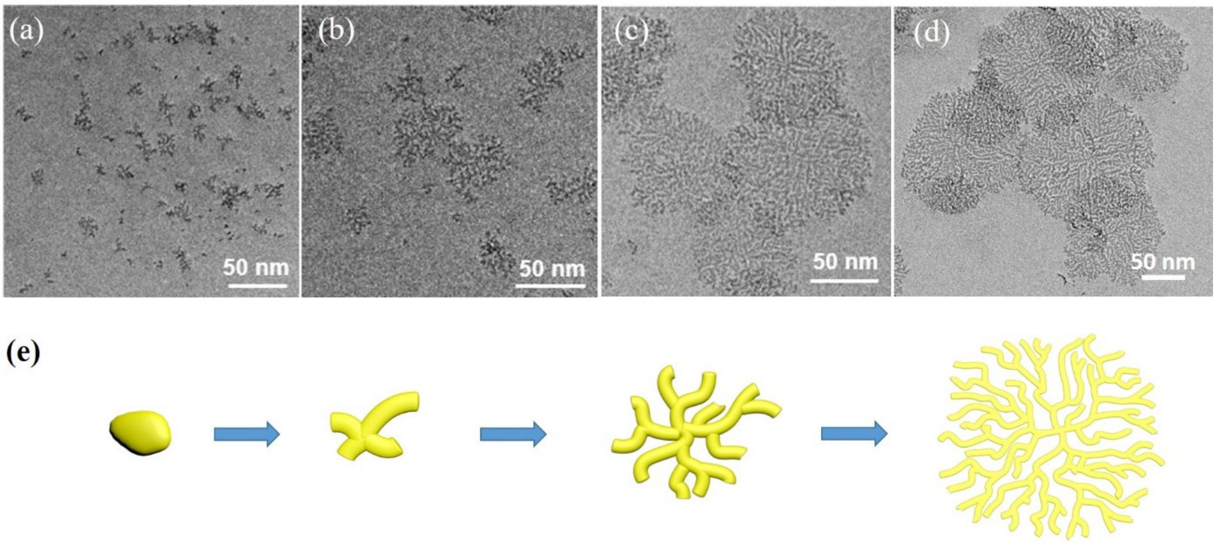

Fig. S5 Typical TEM images of Pt-Ru nanostructures obtained at different crystalline period: (a) 1 h, (b) 2 h, (c) 5h, and (d) 12 h, indicating the continuous epitaxial growth process. (e) The schematic illustration for the epitaxial growth of Pt-Ru crystals.

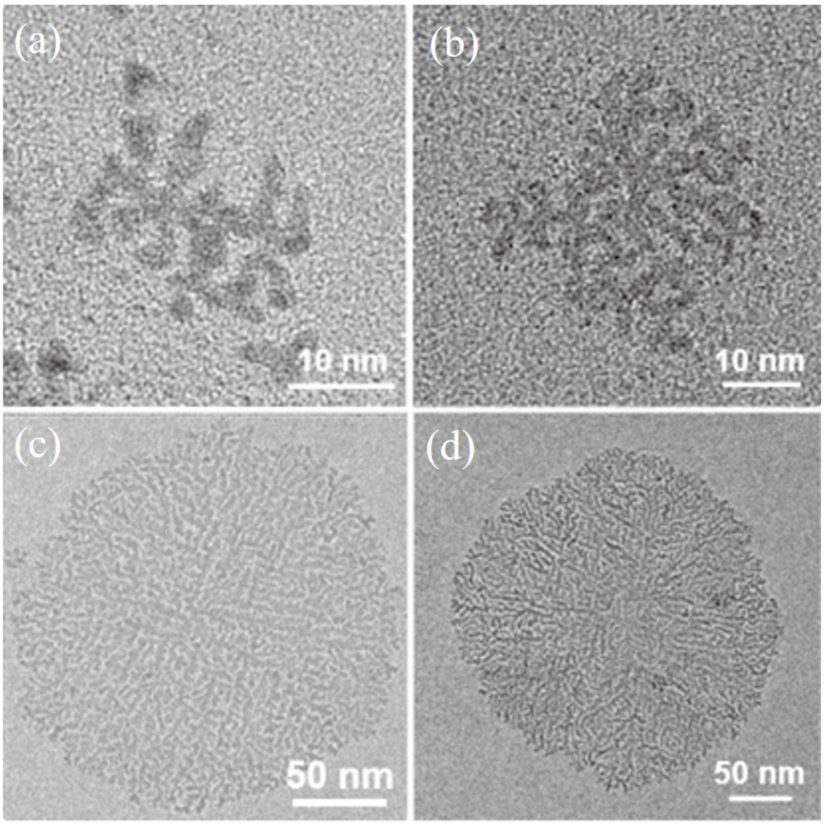

Fig. S6 Typical TEM images of Pt-Ru NDs with different size synthesized under different metallic precursors: (a) ~20 nm, (b) ~40 nm, (c) ~100 nm, and (d) ~300 nm.

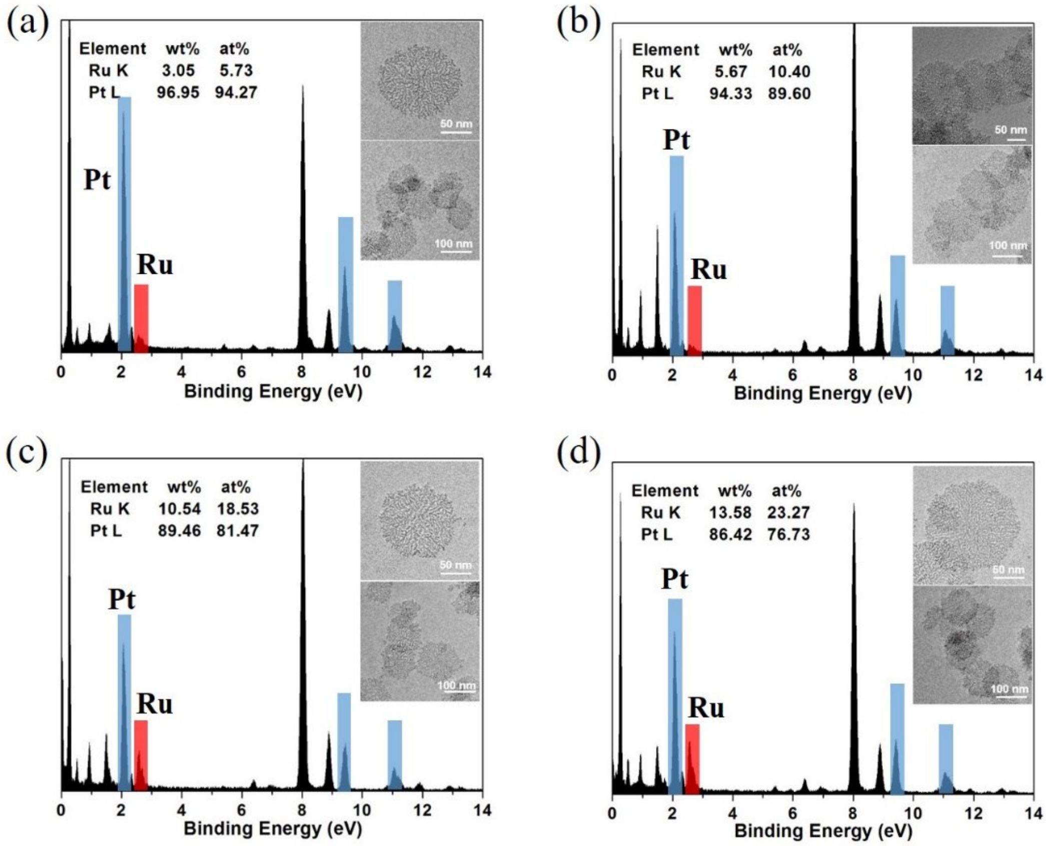

Fig. S7 The EDS of Pt-Ru NDs with different Pt/Ru ratios, (a) $Pt_{95}Ru_5$, (b) $Pt_{90}Ru_{10}$, (c) $Pt_{80}Ru_{20}$, and (d) $Pt_{75}Ru_{25}$. The inserts are the corresponding TEM images of Pt-Ru NDs.

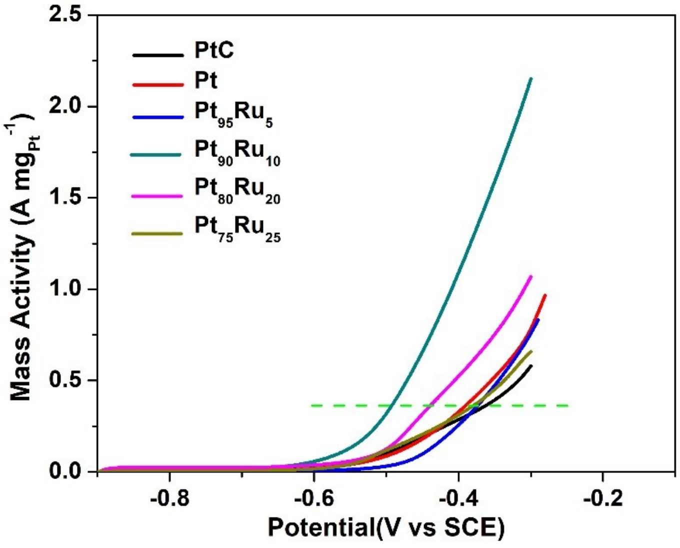

Fig. S8 Linear-sweep voltammograms of Pt, $Pt_{95}Ru_5$, $Pt_{90}Ru_{10}$, $Pt_{80}Ru_{20}$, $Pt_{75}Ru_{25}$ NDs, and commercial PtC collected in 1 M KOH and 1 M methanol at a scan rate of 50 mV s^{-1}.

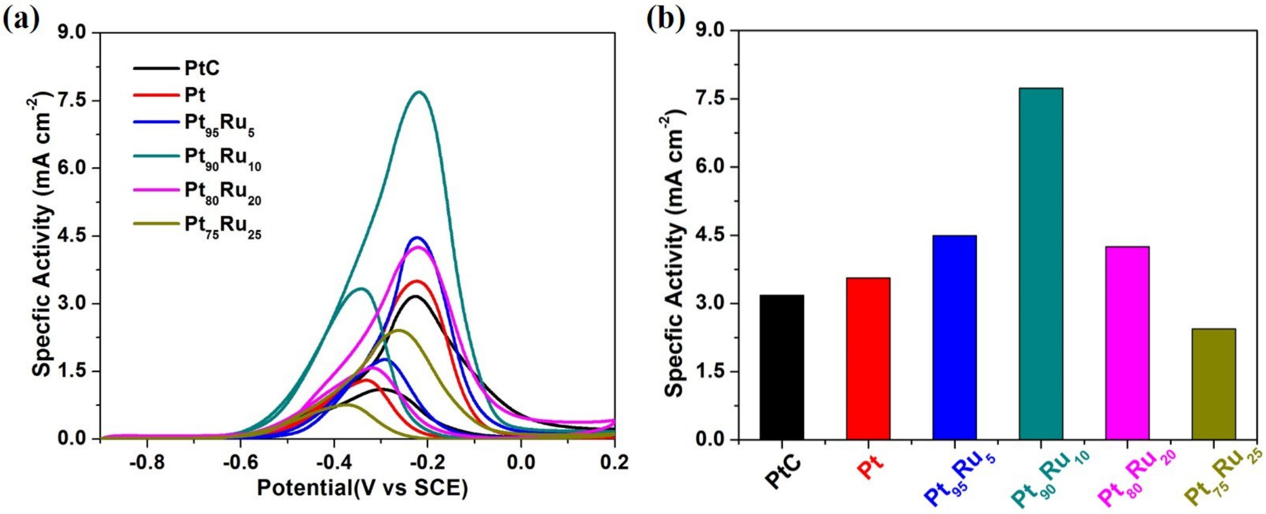

Fig. S9 ECSA-normalized CV curves (a) and summarized activities (b) Pt, $Pt_{95}Ru_5$, $Pt_{90}Ru_{10}$, $Pt_{80}Ru_{20}$, $Pt_{75}Ru_{25}$ NDs, and commercial PtC collected in 1 M KOH and 1 M methanol at a scan rate of 50 mV s^{-1}.

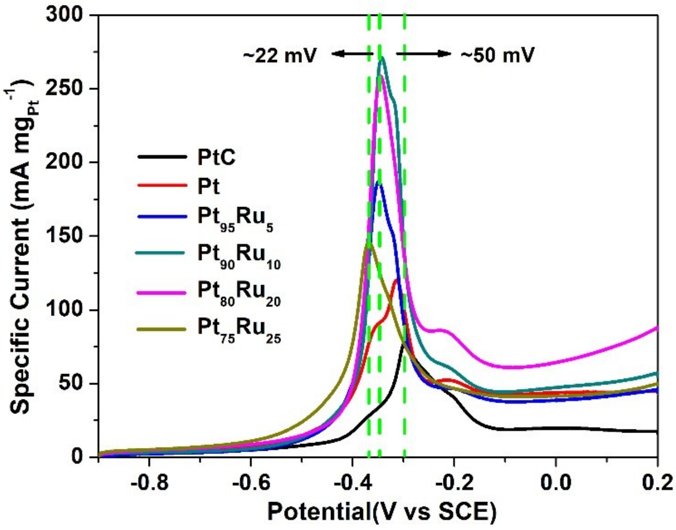

Fig. S10 Comparison of CO stripping voltammograms of Pt, $Pt_{95}Ru_5$, $Pt_{90}Ru_{10}$, $Pt_{80}Ru_{20}$, $Pt_{75}Ru_{25}$ NDs, and commercial PtC collected in 1.0 M KOH at a scan rate of 50 mV s^{-1}.

From the comparison of CO stripping voltammograms, it can be found that $Pt_{95}Ru_5$, $Pt_{90}Ru_{10}$, $Pt_{80}Ru_{20}$ NDs possess similar onset potentials and peak current potentials, obviously more negative than Pt NDs and commercial PtC (~50 mV), but more positive than $Pt_{75}Ru_{25}$ NDs (~22 mV). The more negative onset and peak current potentials in Pt-Ru alloys demonstrated that the surface Ru sites can effectively facilitate the removal of CO_{ads}, indicating the important role of Ru during electrocatalytic MOR process. If only comparing the values of onset and peak current potentials, $Pt_{75}Ru_{25}$ NDs indeed exhibit better CO tolerance capability than other ratios (including $Pt_{90}Ru_{10}$). However, during the i-t chronoamperometry test, the oxidation and leaching of active Pt atoms under high potential may be another important reason for the inactivation of catalyst, although serious surface poisoning by the intermediate species is the main factor. The relatively low electrocatalytic active sites in $Pt_{75}Ru_{25}$ NDs may mainly result in the rapid decay of mass activity. Therefore, although $Pt_{75}Ru_{25}$ NDs exhibit better CO tolerance capability than other Pt/Ru ratios, they still present low electrocatalytic activity and stability, especially compared to $Pt_{90}Ru_{10}$ NDs. As for $Pt_{90}Ru_{10}$ NDs, they hold the largest active area which mainly result in enhanced electrocatalytic activity. The Ru content in $Pt_{90}Ru_{10}$ NDs could be enough to remove the poisoning species during the MOR process, which contribute to the higher activity and stability. In brief, the enhanced electrocatalytic performance (including activity and stability) of $Pt_{90}Ru_{10}$ NDs profit from the synergetic effect of high large active sites and increased CO tolerance capability.

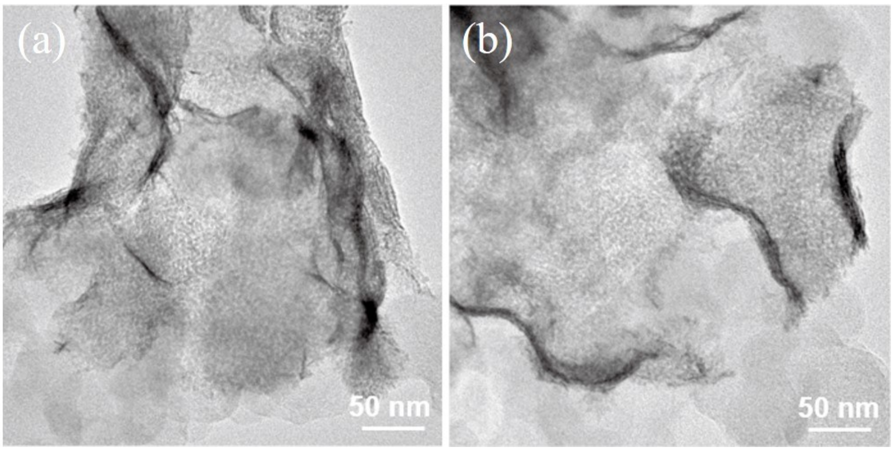

Fig. S11 Representative TEM images of $Pt_{90}Ru_{10}$ NDs before and after the 5000 s electrocatalytic tests.

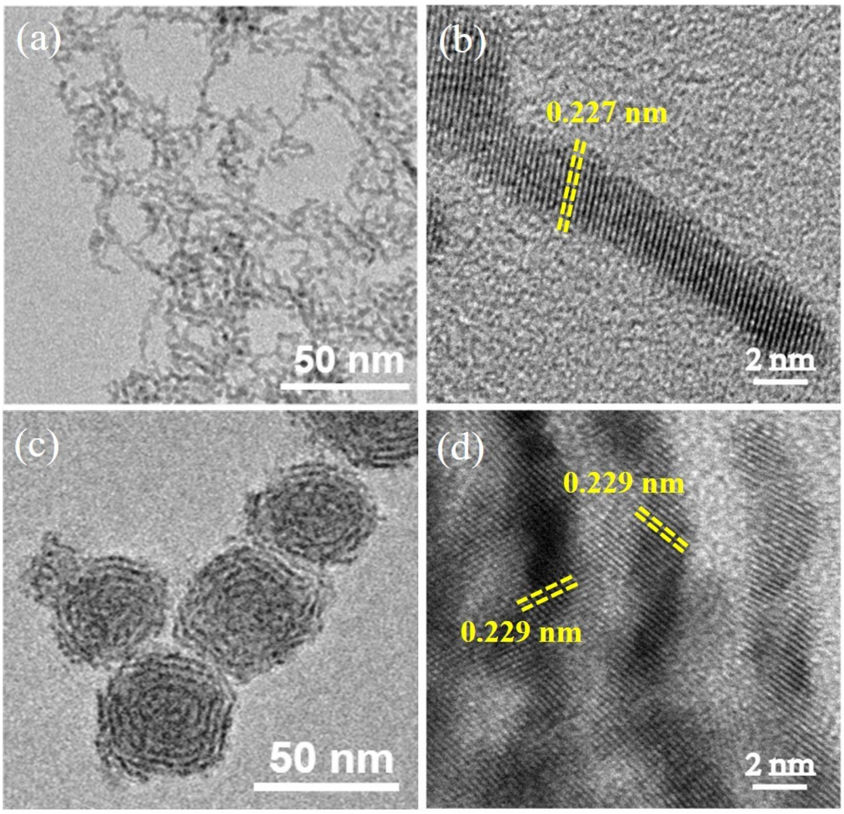

Fig. S12 TEM and HRTEM images of Pt-Ru nanowires (a-b) and nanorings (c-d) with similar atomic ratio to $Pt_{90}Ru_{10}$ NDs.

First, the ultrathin nanodendrites result in more electrocatalytic active sites (e.g., more crystallographic steps, corners, and cavities) and higher atomic efficiency of noble Pt for MOR versus commercial Pt nanoparticles. The structural advantage can be further notarized through the electrocatalytic comparison with other morphologies. For example, Pt-Ru nanowires (NWs) and mesoporous nanorings (NRs) with similar atomic ratios to $Pt_{90}Ru_{10}$ NDs were also synthesized by surfactant-directed aqueous synthesis (Fig. S12). From the results of electrocatalytic MOR (Fig. S13), we could find that $Pt_{90}Ru_{10}$ NDs possess larger ECSA and mass activity compared to $Pt_{90}Ru_{10}$ NWs and NRs, indicating the structural advantage of nanodendritic morphology for MOR. Second, "volcano"-type MOR activities of Pt-Ru NDs with distinct atomic ratios evidenced the compositional effect of Ru content in Pt-Ru alloys to electrocatalytic MOR process. As reported everywhere, the rate-determining step (indirect pathway) in MOR is usually assigned to the adsorption and removal of the poisoning intermediates (CO_{ads} species).[4] Alloyed Ru atoms can efficiently bring in abundant adsorbed OH_{ads} at the lower potential, which would subsequently oxidize the CO_{ads}. Importantly, appropriate distance between Pt and Ru atoms is beneficial to the reactions among Pt-CO_{ads} and Ru-OH_{ads} species.[5] In our 2D Pt-Ru nanostructures with exposed (110) facets, less embedded Ru atoms (e.g., < 10%) only provide insufficient OH_{ads} while more Ru atoms in fcc Pt nanoframework (e.g., > 10%) will occupy Pt active sites, both resulting in the declines in electrocatalytic activities. In brief, the enhanced electrocatalytic performance can be only reached in Pt-Ru nanostructures with ultrathin architecture and specific Pt/Ru ratio. Similar trend about electrocatalytic activities were also observed in acidic solution (Fig. S14 and Table S2).

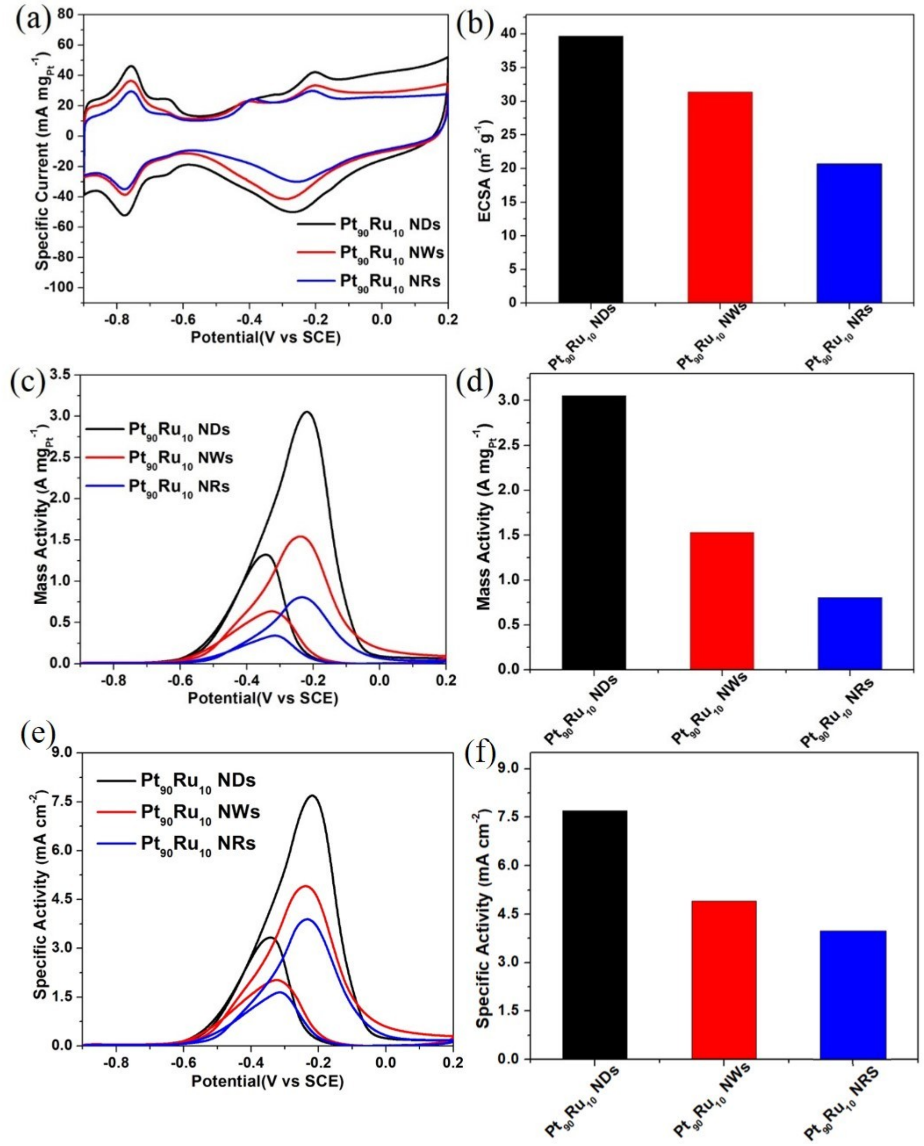

Fig. S13 CV curves (a) and calculated ECSAs (b) of $Pt_{90}Ru_{10}$ NDs, NWs, and NRs. CV curves (c) and summarized mass activities (d) of $Pt_{90}Ru_{10}$ NDs, NWs, and NRs in 1.0 M KOH and 1.0 M methanol. ECSA-normalized CV curves (e) and summarized activities (f) of $Pt_{90}Ru_{10}$ NDs, NWs, and NRs in 1.0 M KOH and 1.0 M methanol.

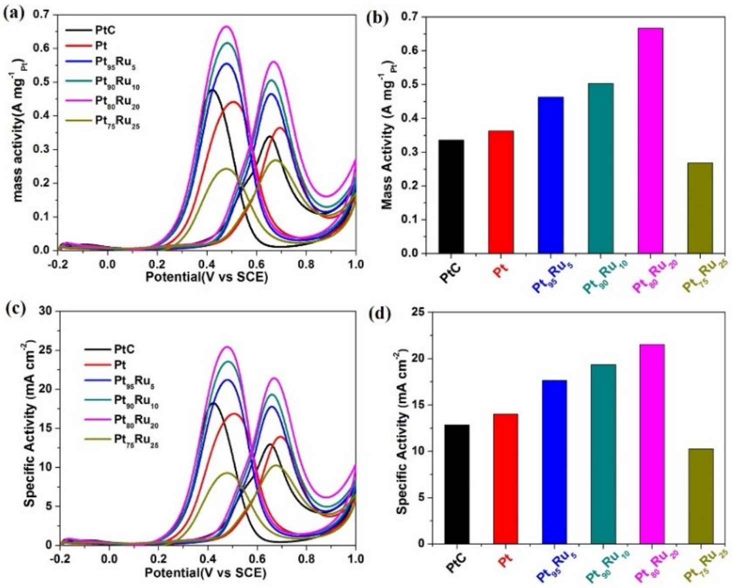

Fig. S14 Mass activities (a) and summarized mass activities (b), specific activity (c) and summarized specific activities (d) of Pt, $Pt_{95}Ru_5$, $Pt_{90}Ru_{10}$, $Pt_{80}Ru_{20}$, $Pt_{75}Ru_{25}$ NDs, and commercial PtC in 1.0 M CH_3OH and 0.5 M H_2SO_4 solution.

The electrocatalytic MOR performance of obtained Pt-Ru alloys was also checked in the acidic solution. From the CV curves, the mass activities of Pt, $Pt_{95}Ru_5$, $Pt_{90}Ru_{10}$, $Pt_{80}Ru_{20}$, $Pt_{75}Ru_{25}$ NDs, and commercial PtC were measured to be 0.365, 0.466, 0.508, 0.563, 0.269, and 0.342 A mg_{Pt}^{-1}, respectively. Obviously, slightly different with the results obtained in alkaline solution, ultrathin $Pt_{80}Ru_{20}$ NDs exhibited relatively enhanced MOR activity, 1.1-2.1 times higher than other Pt/Ru ratios, and 1.6 times than commercial PtC. Additionally, $Pt_{80}Ru_{20}$ NDs also presented more negative onset oxidation potential compared to other nanocrystals (superior methanol oxidation kinetics). The different trend may be caused due to the relative difficulty for the formation of surface OH_{ads} in acidic solution compared to alkaline solution. In acidic condition, more Ru sites are favorable to produce enough Ru-OH_{ads} species. Therefore, $Pt_{80}Ru_{20}$ NDs presented better MOR activity than $Pt_{90}Ru_{10}$ NDs. When increasing the Ru content (e.g., more than 25%), more Ru atoms in fcc Pt nanocrystals would occupy Pt active sites, resulting in the declines in electrocatalytic activities. The general trend of electrocatalytic activities hold the similar law but with some obvious distinction. Additionally, the specific activities follow the same trend as mass activities (c and d). A comparison about the electrocatalytic activities with other reported Pt-Ru or related nanomaterials was provided in revised Table S2. The specific activities are obviously larger than selected cases although the mass activities are not the best.

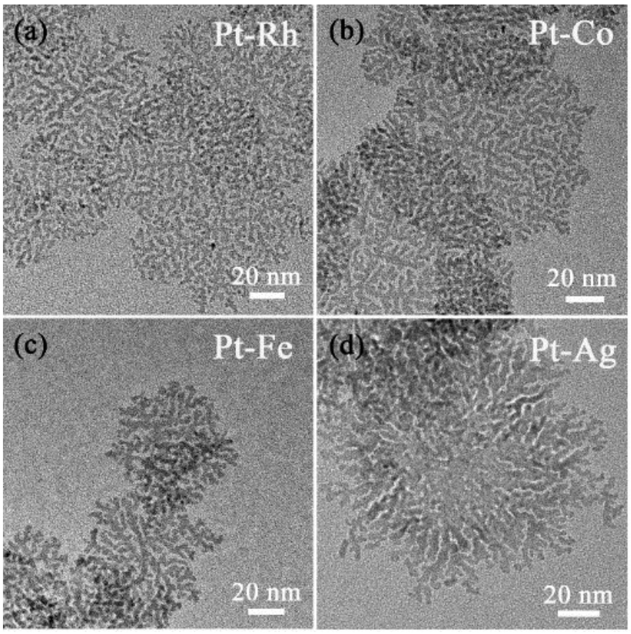

Fig. S15 Typical TEM images of ultrathin Pt-M NDs synthesized by surfactant C22N-COOH, (a) Pt-Rh, (b) Pt-Co, (c) Pt-Fe, and (d) Pt-Ag.

Furthermore, to evaluate the universality of our synthetic strategy for ultrathin Pt-based alloy nanodendrites, bimetallic Pt-M NDs were successfully obtained following similar synthetic procedures by C_{22}N-COOH. Fig. S15 presented representative TEM images of Pt-M NDs with different secondary metals (e.g., Rh, Co, Fe, Ag), all of which exhibited well-defined ultrathin nanodendrites and alloyed framework (Fig. S16 and 17). This facile yet powerful strategy is also expected to produce multimetallic Pt-based alloys in our future work. The electrocatalytic MOR activities of these bimetallic NDs were checked and compared to $Pt_{90}Ru_{10}$ NDs. Similarly, $Pt_{90}Ru_{10}$ NDs performed the largest mass activities (Fig. S18), further proving that secondary oxophilic Ru is the best choice for electrocatalytic MOR.

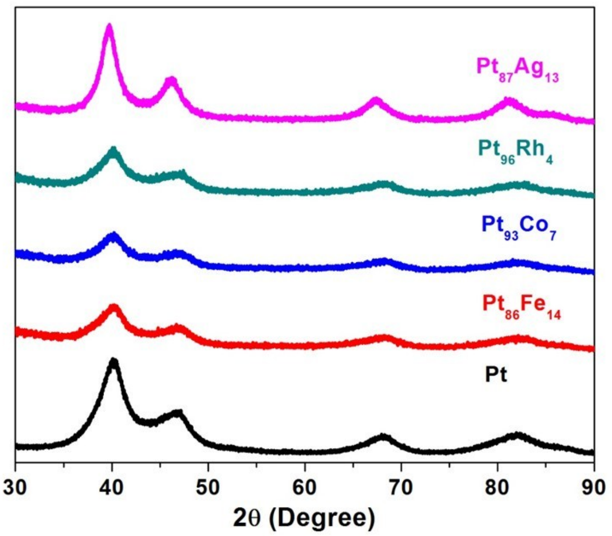

Fig. S16 Wide-angle XRD patterns of ultrathin Pt-Rh, Pt-Co, Pt-Fe, and Pt-Ag NDs.

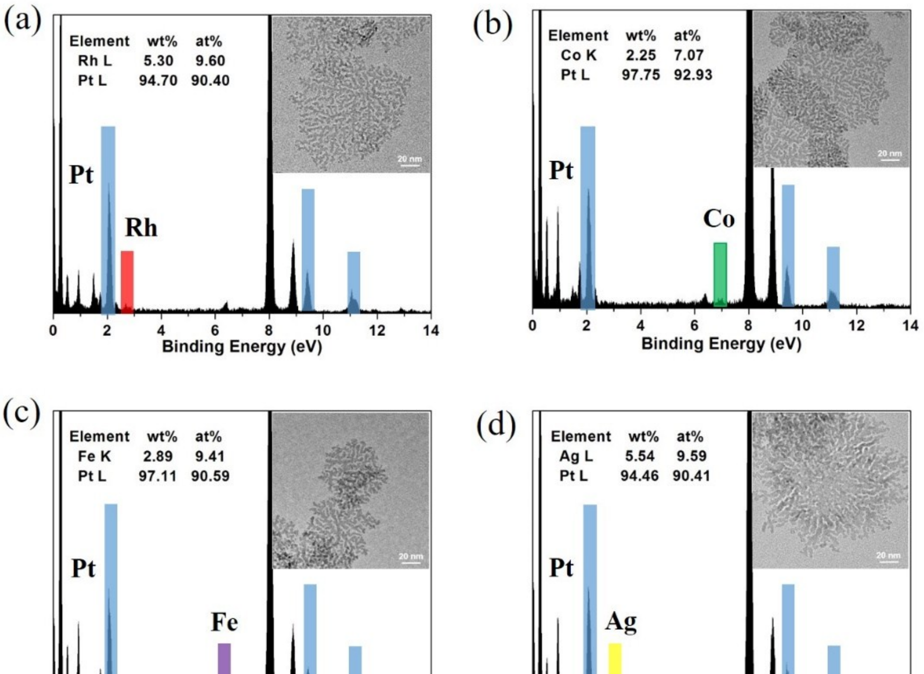

Fig. S17 The EDS of Pt-M NDs, (a) $Pt_{90}Rh_{10}$, (b) $Pt_{93}Co_7$, (c) $Pt_{91}Fe_9$, and (d) $Pt_{90}Ag_{10}$. The inserts are the corresponding TEM images of Pt-M NDs.

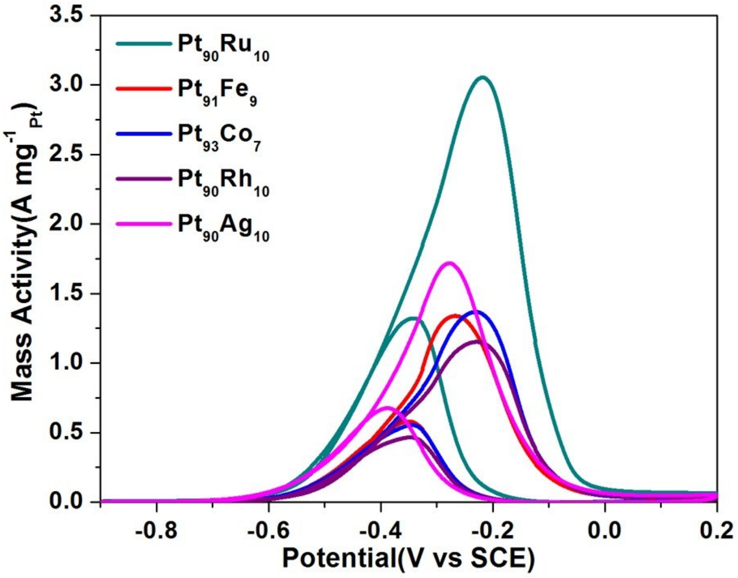

Fig. S18 CV curves of Pt$_{90}$Ru$_{10}$, Pt$_{90}$Rh$_{10}$, Pt$_{93}$Co$_{7}$, Pt$_{91}$Fe$_{9}$, and Pt$_{90}$Ag$_{10}$ NDs collected in 1.0 M KOH and 1.0 M methanol, indicating the larger mass activity of Pt$_{90}$Ru$_{10}$ NDs.

Table S1. Summarization of electrochemical MOR activities of Pt-Ru or related nanocatalysts in alkaline solution.

Materials	Mass activity (A mg^{-1}_{Pt})	Specific activity (mA cm^{-2})	ECSA (m^2 g^{-1})	Electrolyte	Scan rate	Reference
PtRu NDs	**3.06**	**123**	**39.7**	**1.0 M KOH + 1.0 M CH_3OH**	**50 mV/s**	**This work**
Pt_2Ru	-[a]	24	80.71	1.0 M KOH + 1.0 M CH_3OH	50 mV/s	*J. Phys. Chem. C* **2016,** *120*, 6569-6576.
$Pt_{0.3}Ru_{0.6}Pd_{0.1}$	1.042	1.56	67.036	1.0 M KOH + 1.0 M CH_3OH	50 mV/s	*New J. Chem.* **2017,** *41*, 3048-3054.
GC/ILC/PtRu	-	146.9	-	0.5 M KOH + 0.5 M CH_3OH	50 mV/s	*Int. J. Electrochem. Sci.* **2017**, 11271-11286.
N-doped PtRu/C	-	390	51.5	2.0 M NaOH + 2.0 M CH_3OH	50 mV/s	*ChemSusChem* **2014,** *7*, 1854-7.
PtRuBi/C	-	297.1	-	1.0 M KOH + 1.0 M CH_3OH	50 mV/s	*J. Am. Chem. Soc.* **2013,** *135*, 15706-9.
PtCu NFs	2.26	18.2	12.4	0.5 M KOH +1 M CH_3OH	50 mV/s	*Adv. Mater.* **2016,** *28*, 8712-8717.
Pt~Pd_7Cu_3	-	23.2	55.9	1 M CH_3OH + 1 M NaOH	20 mV/s	*ACS Appl. Mater. Interfaces* **2015,** *7*, 26145-26157.
AgAu@Pt nanoframes	0.4831	1.96	24.6	0.2 M KOH + 1.0 M CH_3OH	50 mV/s	*Nanoscale* **2018,** *10*, 2231-2235.
Pt/CNTs + CeO_2 H_2O	2.304	-	-	1.0 M KOH + 1.0 M CH_3OH	20 mV/s	*J. Mater. Chem. A* **2018,** *6*, 2318-2326.
Pt_2Ru	-	24	80.71	1.0 M KOH + 1.0 M CH_3OH	50 mV/s	*J. Phys. Chem. C* **2016,** *120*, 6569-6576.
porous Pt NTs	2.33	-	47.17	1.0 M KOH + 1.0 M CH_3OH	50 mV/s	*ACS Appl. Mater. Interfaces* **2016,** *8*, 16147-16153.
PdAu/C	0.9506	-	-	1.0 M KOH + 1.0 M CH_3OH	50 mV/s	*J. Mater. Chem. A* **2013,** *1*, 9157-9163.
Pt/Ni$(OH)_2$/rGO	1.236	150	64.1	1.0 M KOH + 1.0 M CH_3OH	-	*Nat. Commun.* **2015,** *6*, 10035.
PdRu/NiZn oxyphosphides	1.739	4.5	38.7	1.0 M KOH + 1.0 M CH_3OH	50 mV/s	*Nanoscale* **2018,** *10*, 12605-12611.

[a]not mentioned.

Table S2. Summarization of electrochemical MOR activities of Pt-Ru or related nanocatalysts in acidic solution.

Materials	Mass activity (mA mg$^{-1}{}_{Pt}$)	Specific activity (mA cm^{-2})	ECSA (m^2 g^{-1})	Electrolyte	Scan rate	Reference
$Pt_{80}Ru_{20}$ NDs	**563.2**	**21.5**	**39.7**	**0.5 M H_2SO_4 + 1 M CH_3OH**	**50 mV/s**	**This work**
PtRuCu hexapods/C	1350	-[a]	34.57	0.1 M $HClO_4$ + 1 M CH_3OH	50 mV/s	*ACS Catal.* **2018**, *8*, 7578-7584.
RuPtCu ternary alloy	1730	4.59	57.85	0.1 M $HClO_4$ + 1 M CH_3OH	50 mV/s	*Nanoscale* **2018**, *10*, 21178-21185.
PtRu NWs	820	1.16	72.1	0.1 M $HClO_4$ + 1 M CH_3OH	50 mV/s	*J. Am. Chem. Soc.* **2018**, *140*, 1142-1147.
Pt3Ru/Ru	348	-	-	0.5 M H_2SO_4 + 1 M CH_3OH	50 mV/s	*Appl. Surf. Sci.* **2018**, *433*, 279-284.
flowerlike $Pt_{72}Ru_{28}$	1700	10.98	-	0.1 M $HClO_4$ + 0.5 M CH_3OH	50 mV/s	*Adv. Energy Mater.* **2017**, *7*, 1601593.
PtRu nanodendrites	1080	2.7	47.7	0.5 M H_2SO_4 + 1 M CH_3OH	50 mV/s	*Nanoscale* **2017**, *9*, 1033-1039.
$Pt_{17}Pd_{16}Ru_{22}Te_{45}$ NTs	1261.5	2.96	-	0.5 M H_2SO_4 + 1 M CH_3OH	50 mV/s	*J. Am. Chem. Soc.* **2017**, *139*, 5890-5895.
PtRu/TiWC NPs	-	~1.8	-	0.1 M $HClO_4$ + 1 M CH_3OH	50 mV/s	*Science* **2016**, 352, 974.

[a]not mentioned.

Reference

1 D. Xu, X. Liu, H. Lv, Y. Liu, S. Zhao, M. Han, J. Bao, J. He and B. Liu, *Chem. Sci.*, 2018, **9**, 4451-4455.

2 D. Xu, H. Lv, H. Jin, Y. Liu, Y. Ma, M. Han, J. Bao and B. Liu, *J. Phys. Chem. Lett.*, 2019, **10**, 663-671.

3 H. Yang, Y. Tang and S. Zou, *Electrochem. Commun.*, 2014, **38**, 134-137.

4 D. J. Chen and Y. J. Tong, *Angew. Chem. Int. Ed.*, 2015, **54**, 9394-9398.

5 L. Zhuang, J. Jin and H. D. Abruña, *J. Am. Chem. Soc.*, 2007, **129**, 11033-11035.